ACS APPLIED MATERIALS & INTERFACES

Research Article

Cite This: ACS Appl. Mater. Interfaces 2019, 11, 7954−7964

www.acsami.org

Thermodynamic Overpotentials and Nucleation Rates for Electrodeposition on Metal Anodes

Kyle S. Nagy,[†,⊥] Saeed Kazemiabnavi,[†,⊥] Katsuyo Thornton,[‡,§,∥,⊥] and Donald J. Siegel*[,†,‡,§,∥,⊥]

[†]Mechanical Engineering Department, [‡]Materials Science and Engineering, [§]Applied Physics Program, [∥]University of Michigan Energy Institute, and [⊥]Joint Center for Energy Storage Research, University of Michigan, Ann Arbor, Michigan 48109, United States

Supporting Information

ABSTRACT: Rechargeable batteries employing metal negative electrodes (i.e., anodes) are attractive next-generation energy storage devices because of their greater theoretical energy densities compared to intercalation-based anodes. An important consideration for a metal's viability as an anode is the efficiency with which it undergoes electrodeposition and electrodissolution. The present study assesses thermodynamic deposition/dissolution efficiencies and associated nucleation rates for seven metals (Li, Na, K, Mg, Ca, Al, and Zn) of relevance for battery applications. First-principles calculations were used to evaluate thermodynamic overpotentials at terraces and steps on several low-energy surfaces of these metals. In general, overpotentials are observed to be the smallest for plating/stripping at steps and largest at terrace sites. The difference in the coordination number for a surface atom from that in the bulk was found to correlate with the overpotential magnitude. Consequently, because of their low bulk coordination, the body-centered alkali metals (Li, Na, and K) are predicted to be among the most thermodynamically efficient for plating/stripping. In contrast, metals with larger bulk coordination such as Al, Zn, and the alkaline earths (Ca and Mg) generally exhibit higher thermodynamic overpotentials. The rate of steady-state nucleation during electrodeposition was estimated using a classical nucleation model informed by the present first-principles calculations. Nucleation rates are predicted to be several orders of magnitude larger on alkali metal surfaces than on the other metals. This multiscale model highlights the sensitivity of the nucleation behavior on the structure and composition of the electrode surface.

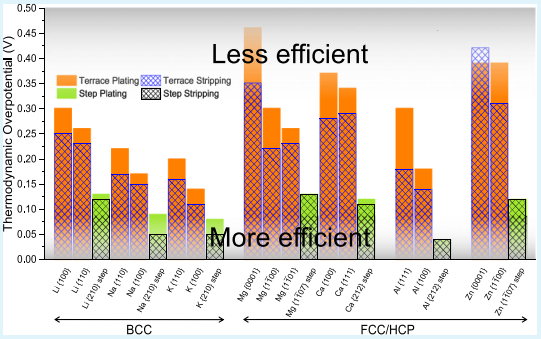

KEYWORDS: *batteries, energy storage, electrodeposition, metal anodes, nucleation, dendrites*

INTRODUCTION

Despite the success of lithium-ion batteries,[1−3] demands for higher gravimetric and volumetric energy densities, greater power output, and longer lifetime are driving research into other battery chemistries "beyond Li ion."[4] In this regard, metals are promising candidates for future battery anodes because they have higher theoretical capacities than the graphite-based, intercalation anodes used in lithium-ion batteries, Table 1. Furthermore, the higher abundance of non-Li metals may result in reduced costs.

The use of metal anodes in rechargeable batteries is not a new idea. Early attempts to commercialize a Li metal-based cell were unsuccessful because of dendrite growth during charging.[8] More recently, Fluidic Energy has commercialized a rechargeable Zn−air battery,[9] while Aurbach et al. developed the first rechargeable battery incorporating a Mg metal anode in 2000.[10] Efforts to improve Mg batteries' capabilities is an active area of research.[2,11,12] Al anodes are currently used in primary batteries,[13] but the use of an aqueous electrolyte limits rechargeability because of the irreversibility of the Al_2O_3 discharge product. Plating and stripping Al metal anodes using organic-based electrolytes has been largely unsuccessful at room temperature,[14−16] with ionic liquids demonstrating the only evidence to date of cycling.[17−19] Na batteries using molten Na electrodes have been proposed for applications in load-leveling and emergency power.[3] Nevertheless, consid-

Table 1. Properties of Candidate Negative Electrode Metals for Use in Battery Applications

anode	abundance (ppm)[5]	gravimetric capacity (mA h/g)	volumetric capacity (mA h/cc)	potential vs SHE (V)[6]
Al	83 176	2980	8046	−1.66
Ca	52 481	1337	2046	−2.87
Mg	32 359	2205	3837	−2.37
Na	22 909	1166	1181	−2.71
K	9120	685	624	−2.93
Zn	79	820	5846	−0.76
Li	13	3862	2093	−3.04
graphite[7]		300−350	790	−2.79 to −2.94

Received: November 10, 2018
Accepted: January 30, 2019
Published: January 30, 2019

DOI: 10.1021/acsami.8b19787
ACS Appl. Mater. Interfaces 2019, 11, 7954−7964

erable interest in room-temperature Na metal anode batteries also exists, as evidenced by numerous studies on Na-ion, Na−O_2 and Na−S systems.[3,20−22] Ren and Wu reported a K−O_2 battery which showed a low discharge/charge voltage gap of less than 50 mV during the initial cycle,[23] and Zhao et al. reported a K−S battery with impressive initial charge capacity.[24] Earlier attempts to cycle Ca anodes in organic-based solvents proved unsuccessful;[25] however, cycling of Ca metal was recently reported at elevated temperatures[26] and at room temperature.[27]

These developments have stimulated growing interest in batteries that employ metallic negative electrodes. To be viable, metal electrodes should undergo electrodeposition (ED) and -dissolution with low overpotentials. For some metals, these processes are highly efficient, yet for others, achieving efficient cycling is a greater challenge. For example, Table S1 lists overpotentials extracted from cyclic voltammograms reported in the literature. These data suggest the existence of trends across the various metals. ED involving Group I metals, such as Li, Na, and K, is the most efficient, whereas ED of Ca is much less. Mg, Al, and Zn tend to fall between these extremes, with their performance dependent on the electrolyte composition, scan rate, and temperature. (e.g., Zn plating/stripping is typically efficient in aqueous electrolytes, but is less efficient in nonaqueous systems).[28,29]

These observations beg the question: Why are some metals able to plate and strip more easily than others? The overpotentials associated with ED and -dissolution provide a measure of the efficiency of these processes. In general, these overpotentials can be traced to four contributing processes: charge transfer, mass transport, chemical reaction, and crystallization.[30] As a step toward understanding efficiency differences between different metal electrodes, the present study uses first-principles calculations to evaluate "thermodynamic overpotentials (TOs)"[31] associated with plating and stripping on several low-energy surfaces of seven metals relevant for battery applications: Li, Na, K, Mg, Ca, Al, and Zn. Reactions at terraces and step edges are considered. The thermodynamic factors probed here contribute to the reaction and crystallization components of overpotentials and reflect heterogeneity in the adsorption/desorption energy of ions arising from inequivalent reaction sites on the electrode surface.

We find that the magnitude of the calculated overpotentials is in many cases similar to measured values, and ranges from tens to hundreds of mV. These calculations also capture the inefficiencies (i.e., large overpotentials) associated with ED of Ca and Mg; the calculated TOs for these metals are amongst the largest overall, which is consistent with measurements (summarized in Table S1). We observe that a metal's crystal structure correlates with plating and stripping efficiency; the body-centered cubic alkali metals are predicted to be among the most efficient, whereas the remaining metals, all of which possess face-centered cubic or hexagonal close-packed crystal structures, are predicted to have higher TOs. As expected, ED/dissolution is most efficient at kink sites on steps,[32] while terrace sites yield the largest TOs. Quantitative differences between the calculated and experimentally measured overpotentials point toward the importance of kinetic factors, such as Ohmic resistance in electrolytes, diffusion through solid electrolyte interphases, surface diffusion, electron transfer, etc. These factors are not accounted for in the thermodynamic analysis presented here.

Recognizing that the rate and density of nucleation can affect the evolution of electrodeposits,[33−36] steady-state nucleation rates are estimated using a multiscale approach wherein a classical nucleation model is informed by the present density functional theory (DFT) calculations.[37−39] These simulations allow for a comparison of nucleation rates during ED on different metallic surfaces and surface features (e.g., terraces vs step edges). The small TOs predicted for plating at step edges result in higher nucleation rates at these features, suggesting that a large population of kink sites will promote efficient cycling. Nucleation rates on terraces differ by several orders of magnitude across the metals, with rates on the body-centered cubic metals predicted to be the fastest. In contrast, nucleation rates at step edges are within a few orders of magnitude of each other, indicating a relatively weak dependence on metal composition.

METHODOLOGY

DFT calculations[40] were performed using the Vienna Ab-initio Simulation Package (VASP).[41−44] The Perdew−Burke−Ernzerhof formulation of the generalized gradient approximation[45] (GGA-PBE) was used for exchange−correlation effects, and Blöchl's projector augmented wave method[46] was used to describe interactions between the core and valence electrons. The plane-wave energy cutoff was set to 350 eV for all systems; convergence testing revealed that this cutoff was sufficient to achieve energy convergence to within 1 meV per atom. The electronic self-consistent iterations were discontinued when the change in total energy and the change in energy eigenvalues were both within 10^{-6} eV. Hellmann−Feynman forces were converged to within 0.02 eV/Å.

Convergence testing was performed on the primitive cells of the bulk metallic crystals to determine the optimal sizes of the Γ-centered k-point meshes. Energy convergence to within 1 meV per atom was achieved for k-point grids of density 34^3 for Al, 16^3 for Ca, 16^3 for K, 28^3 for Li, 20^3 for Mg, 16^3 for Na, and 27^3 for Zn. For surface cells used in surface energy calculations and for expanded surface supercells used in the adsorption energy calculations, Γ-centered k-point meshes of round $(k_0a_0/a) \times$ round $(k_0a_0/b) \times 1$ were used, where k_0 is the k-point grid dimension for the primitive cell, a_0 is the primitive cell lattice parameter (the basal plane lattice parameter in the case of the HCP metals), and a and b represent the in-plane lattice parameters of the surface cell.

During ED, atoms absorbed onto the electrode surface may subsequently diffuse to join other atoms, forming both stable and unstable clusters; some of these clusters then grow and ultimately form an electrodeposited film. The growth of a cluster is described as the sequential addition of individual atoms. The critical nucleus size is defined as the minimum size above which nuclei will spontaneously grow. Below the critical nucleus size, clusters dissolve with high probability.[47]

According to classical nucleation theory,[48,49] the time-dependent nucleation rate, $J(t)$, can be expressed in terms of induction time, τ, and the steady-state nucleation rate, J_0, using eq 1[48]

$$J(t) = J_0\left[1 + 2\sum_{n=1}^{\infty}(-1)^n \exp\left(\frac{-n^2 t}{\tau}\right)\right] \quad (1)$$

where J_0 is expressed as[47]

DOI: 10.1021/acsami.8b19787
ACS Appl. Mater. Interfaces 2019, 11, 7954−7964

Table 2. Calculated Surface Energies (σ) for a Given *hkl* Surface Facet with and without Corrections (Described in refs 63 and 64), the Equilibrium Area Fraction of Each Facet as Determined by the Wulff Construction, and the Area-Weighted Surface Energy, $\sigma_{weighted}$

metal	{*hkl*}	σ uncorrected (J/m^2)	σ corrected (J/m^2)	other calculations (J/m^2)	area fraction	$\sigma_{weighted}$ (J/m^2)	expt. values (J/m^2)
Al	{100}	0.92	1.05	0.93,[53] 0.92[54]	0.17	1.01	1.14,[55] 1.16,[56] 1.14[57]
	{110}	1.01	1.14	1.03,[53] 0.98[54]	0.02		
	{111}	0.82	0.96	0.83,[53] 0.80[54]	0.57		
	{120}	0.99	1.13	1.02[54]	0.09		
	{113}	0.96	1.09	0.98[54]	0.15		
	{133}	0.99	1.12	0.96[54]			
Ca	{100}	0.46	0.49	0.53,[58] 0.44,[59] 0.46[54]	0.43	0.50	0.50,[55] 0.49,[56] 0.37[57]
	{110}	0.55	0.58	0.64,[58] 0.52,[59] 0.54[54]			
	{111}	0.47	0.50	0.55,[58] 0.44,[59] 0.46[54]	0.57		
	{120}	0.55	0.59	0.55[54]			
	{113}	0.54	0.57	0.53[54]			
	{133}	0.53	0.56	0.53[54]			
Li	{100}	0.45	0.49	0.54,[58] 0.46,[60] 0.46[54]	0.33	0.52	0.52,[55] 0.53,[56] 0.53[57]
	{110}	0.49	0.53	0.59,[58] 0.49,[60] 0.50[54]	0.33		
	{111}	0.53	0.56	0.60,[58] 0.53,[60] 0.54[54]	0.04		
	{114}	0.52	0.55				
	{120}	0.51	0.54	0.51[54]	0.13		
	{121}	0.54	0.57	0.54[54]	0.06		
	{233}	0.53	0.57	0.52[54]	0.10		
Na	{100}	0.23	0.24	0.26,[58] 0.22,[60] 0.22[54]	0.20	0.24	0.26,[55] 0.26,[56] 0.24[57]
	{110}	0.21	0.23	0.25,[58] 0.22,[60] 0.22[54]	0.67		
	{111}	0.23	0.25	0.30,[58] 0.26,[60] 0.25[54]	0.09		
	{114}	0.25	0.26				
	{120}	0.29	0.30	0.23[54]			
	{121}	0.24	0.26	0.27[54]	0.04		
	{233}	0.25	0.26	0.25[54]			
K	{100}	0.12	0.12	0.15,[58] 0.12[54]	0.17	0.11	0.15,[55] 0.13,[56] 0.13[57]
	{110}	0.11	0.11	0.14,[58] 0.11[54]	0.77		
	{111}	0.13	0.13	0.17,[58] 0.13[54]	0.01		
	{114}	0.13	0.13				
	{120}	0.12	0.13	0.12[54]			
	{121}	0.12	0.13	0.13[54]	0.05		
	{233}	0.13	0.13	0.13[54]			
Mg	{001}	0.53	0.59	0.52,[60] 0.54[54]	0.17	0.69	0.79,[55] 0.76,[56] 0.47[57]
	{1$\bar{1}$0}	0.63	0.70	0.60[54]	0.37		
	{1$\bar{1}$1}	0.65	0.71	0.63[54]	0.46		
	{110}	0.78	0.85	0.72[54]			
	{111}	0.78	0.84	0.76[54]			
Zn	{001}	0.32	0.41	0.35[54]	0.46	0.57	0.99,[55] 0.99,[56] 0.92[57]
	{1$\bar{1}$0}	0.61	0.71	0.53[54]	0.54		
	{1$\bar{1}$1}	0.71	0.80	0.70[54]			

$$J_0 = N\left(\frac{\omega_c}{g_c}\right)\left(\frac{\Delta G_c}{3\pi k_B T}\right)^{1/2}\exp\left(\frac{-\Delta G_c}{k_B T}\right) \quad (2)$$

Here, N is the total number of atoms per unit surface area of the electrode that can contribute to the formation of nuclei. Assuming that a layer of the electrolyte in the vicinity of the electrode contributes directly to the nucleation, N can be calculated using $N = N_A \cdot C_0 \cdot d$, where N_A is Avogadro's number, C_0 is the electrolyte concentration (1000 mol/m^3), and d is the thickness of the layer of the electrolyte in the vicinity of the electrode (assumed 10 Å for all cases). ΔG_c is the formation energy of the critical nucleus, g_c is the number of atoms in the critical nucleus, and ω_c is the frequency of collision of the atoms with the critical nucleus.

In classical nucleation theory, the formation energy of the cluster is assumed to be separable into bulk free energy and surface free energy terms. This assumption holds as long as the cluster is large enough to distinguish between its surface and bulk regions. However, very small clusters do not satisfy these criteria; the cluster does not necessarily take the crystal structure of the bulk phase, and no clear differentiation between the bulk and surface energy contributions can be made. Therefore, an atomistic approach is necessary to determine the formation energies of clusters that are on the nanoscale. As described below, the deposition of the first adatom on the electrode surface is consistently the most endergonic or "uphill" ED step, independent of the surface composition or structure (terrace or step). This behavior suggests that the critical cluster size should be taken as a single atom. Similarly, ΔG_c is defined in eq 2 to be the reaction energy of the deposition of the initial adatom at either a terrace or a step.

DOI: 10.1021/acsami.8b19787
ACS Appl. Mater. Interfaces 2019, 11, 7954−7964

RESULTS AND DISCUSSION

Bulk Properties. The lattice constants and bulk moduli for Al, Ca, K, Li, Mg, Na, and Zn were calculated and compared with experimental and computational values reported in the literature. Primitive cells of the metals were relaxed until the structure that minimized the total energy was achieved. The bulk moduli were calculated using a series of fixed-volume cells, allowing the lattice and basis vectors of each to relax and fitting the total energy versus volume data to the Murnaghan equation of state.[50] Table S2 lists the resulting lattice constants and bulk moduli, along with experimental values and other calculated values. There is excellent agreement between our calculated lattice vectors, experimental measurements, and those reported from other calculations which used the GGA-PBE exchange−correlation functional; in all cases, the disagreement is ∼2% or less. Similarly, less than 10% disagreement is observed between the calculated and measured bulk moduli. (One exception is Zn, which as noted in Ledbetter's compilation of Zn properties,[51] could be because of its relatively high anisotropy.)

To avoid spurious errors resulting from the differences in *k*-point sampling sets between the surface and bulk simulation cells, the energies of the atoms in the bulk were calculated according to the method of Fiorentini and Methfessel.[52] Following this method, slab models of varying thicknesses were constructed for the surfaces under consideration. The in-plane surface dimensions were obtained from the bulk lattice parameters calculated previously, while the thicknesses of the slabs were increased sequentially from 10 to 20 layers, maintaining 15 Å of vacuum separation between the surfaces. The total energies from the relaxed cell calculations were plotted versus the number of layers, and the slopes of the linear portions yielded the bulk energies.

Surface Energies and Wulff Plots. In order to identify the most likely surfaces of the metal electrodes to be present during ED, equilibrium crystallite shapes were predicted by constructing Wulff plots from the calculated surface energies of several plausible facets. Surfaces with the largest areal packing densities are typically expected to exhibit the lowest surface energies; thus, our surface energy calculations emphasize these surfaces. Supercells contained slabs of 10−22 layers in thickness, with the free surfaces separated by 20 Å of vacuum. All atoms were relaxed to their minimum force positions. The surface energy was calculated as

$$\sigma = \frac{1}{2A}(E^{\text{slab}} - n_{\text{slab}}\mu^0) \tag{3}$$

where the surface area of the cell is given by $A = |\boldsymbol{a} \times \boldsymbol{b}|$, with $\boldsymbol{a}$ and $\boldsymbol{b}$ as the surface lattice vectors, E^{slab} is the total energy of the slab cell, n_{slab} and n_{bulk} are the number of atoms in the slab and bulk cells, respectively, and μ^0 is the total energy per atom of the bulk cell, calculated using the method described above. The factor of 2 in the denominator accounts for the presence of two surfaces in the slab calculations.

Mattsson and co-workers have discussed an error present in local (local-density approximations, LDA) and semilocal (GGA) DFT calculations on surfaces. This error arises from the rapidly decaying nature of the electron density at the solid−vacuum interface.[61,62] A simple scheme was developed to account for this error,[63,64] which in practice involves adding a correction to the surface energy as calculated with LDA, PBE, or PW91 functionals. We have applied this correction in our GGA-PBE-based surface energy calculations, which are summarized in Table 2. To facilitate comparisons with earlier, noncorrected calculations, our uncorrected surface energies are also reported. As shown in the table, the present (uncorrected) surface energies are in good agreement with earlier calculations.

With these corrected surface energies, equilibrium crystallite shapes (i.e., Wulff plots) were constructed using the Wulffmaker program,[65] Figure 1. In addition to listing the corrected

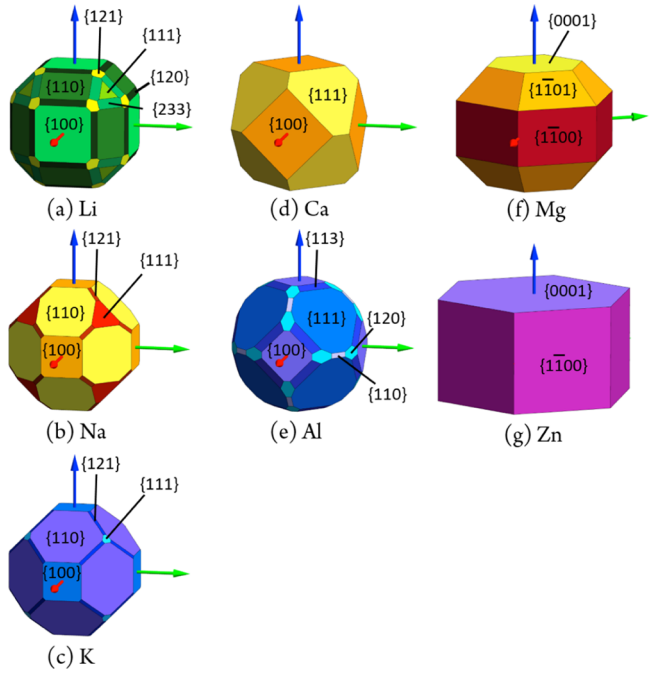

Figure 1. Wulff plots for (a) Li, (b) Na, (c) K, (d) Ca, (e) Al, (f) Mg, and (g) Zn. At ambient conditions, (a−c) adopt the BCC crystal structure, (d−e) adopt the FCC structure, and (f−g) are HCP.

surface energies, Table 2 tabulates the respective fraction of the crystallite surface area of each facet. Based on the surface energies and areas, σ_{weighted} represents the area-weighted average of the surface energy. This value is expected to be the property most closely resembling experimental measurements of the surface energy in the cases where the *hkl* index of the surface is not known. Indeed, less than 12% disagreement was observed between σ_{weighted} and the average of the experimental values for each of Al, Ca, Li, Na, and Mg. The discrepancy between theory and experiment is larger for potassium (∼20%) and Zn (>40%). The absolute values for the surface energy of K are smaller than those for the other metals considered here, and therefore, a small variation yields a greater percentage error. It should also be noted that other calculated surface energies agree well with our calculated surface energies, including those of Zn.

There are several possible explanations for the discrepancies between the experimental and calculated surface energy of Zn, one of which is the experimental method used to obtain the surface energies. For example, Tyson[55] established a linear correlation between cohesive energy at 0 K and surface energy, whereas de Boer et al.[56] established a linear trend between enthalpy of vaporization and surface energy. It has been noted[66,67] that these methods use observables that are referenced to elements in the gas phase, which in the case of

DOI: 10.1021/acsami.8b19787
ACS Appl. Mater. Interfaces 2019, 11, 7954−7964

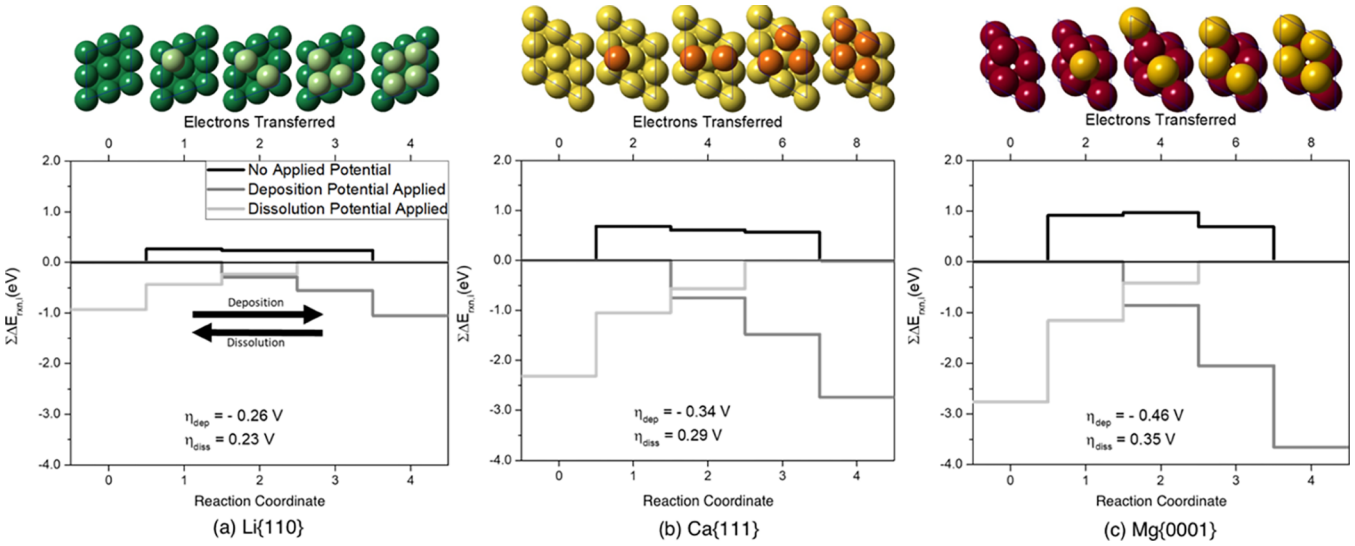

Figure 2. Calculated deposition/dissolution reaction energies on the terraces of three representative metallic anodes: (a) Li{110}, (b) Ca{111}, and (c) Mg{0001}. Deposition energies are read left to right, and dissolution energies are read right to left. Reaction energies are plotted for three scenarios of applied potential, V:$V = E^0$, represented with the black line, corresponds to the equilibrium potential for a given metal; $V = \eta_{dep}$, dark gray line, where η_{dep} is the thermodynamic overpotential for deposition; and $V = \eta_{des}$, light gray line, where η_{des} is the thermodynamic overpotential for desorption. Images above the plots show the state of the simulation cells at each reaction step. Dark green, yellow, and red represent the Li, Ca, and Mg electrode surface atoms, respectively, whereas light green, orange, and yellow represent Li, Ca, and Mg adatoms, respectively.

the divalent metals Hg, Cd, Mg, and Zn, leads to significant errors in the resulting surface energies. Furthermore, the experimental values use surface tensions measured at high temperatures, but then extrapolate to 0 K.[55,66,67] Additionally, several authors[68,69] have noted that experimentally determined surface energies are generally larger than those predicted by calculations. This results from the presence of surface defects, and the experimental surfaces being a mixture of several crystallographic planes.

Overview of Thermodynamic Overpotential Calculations. The calculation of TOs has been used extensively to examine electrocatalysts[70−78] and metal−air batteries.[31,69,79−87] The calculated overpotentials from these studies generally agree well with experimentally observed overpotentials. The present study adopts this methodology to explore overpotential contributions during the ED and -dissolution of metal ions at metallic negative electrodes in batteries. The goal is to examine trends in the TOs as a function of the anode composition and surface structure, the latter including various surface facets and adsorption/desorption sites.

Our calculations consider terrace and step sites on the electrode surface. In prior studies,[31,83] it was observed that application of the TO method at terrace sites alone led to an overestimation of the overpotential; electrochemical reactions at step and kink sites yielded predictions more in line with experimental data. Nevertheless, it has also been suggested[84,86] that at high current densities, the overpotentials resulting from charge transfer at terrace sites can contribute to the overpotential when a large number of terrace sites are available. Additionally, the limited time available for surface diffusion under high current densities implies that not all electrodeposited ions will have sufficient time to migrate to low-energy step/kink sites. Thus, it is reasonable to examine the behavior at both terrace and kink sites.

TOs for ED were calculated for a series of atomic deposition events on several low-energy surfaces of the seven metals shown in Figure 1. Deposition on terrace sites was simulated on 2 × 2 expansions of the surface unit cells. These slabs comprised 5−12 layers, yielding slab thicknesses of 9−12 Å. To assess finite-size effects, additional overpotential calculations were performed on larger 3 × 3 and 4 × 4 expansions of the Mg(0001) terrace unit cell. Only a small change in the calculated values was observed, and compared to the 2 × 2 system, the 3 × 3 overpotential differed by 3.5%, whereas the 4 × 4 system differed by 1.5%. All surfaces were constructed using the calculated lattice parameters of the bulk cells. The facets examined for TOs were those with the largest areal fractions: {111} and {100} for Al and Ca; {110} and {100} for Li, Na, and K; {001}, {1$\bar{1}$0}, and {1$\bar{1}$1} for Mg; and {001} and {1$\bar{1}$0} for Zn. Additionally, deposition was simulated on stepped surfaces comprising 11−20 layers, yielding slabs 9−12 Å thick. Step morphologies were approximated using {210} surfaces for BCC metals, {212} for FCC metals, and {10$\bar{1}$7} for HCP metals. To limit image interactions between kink defects, 5−6 surface unit cells were used in the direction parallel to the step edge.

The energetically preferred adsorption sites were determined by a search over possible sites on each surface. This energy was recorded, and subsequent deposition reactions were evaluated in the presence of the adsorbate(s) produced in earlier steps. Each configuration was allowed to relax until it met the force convergence criterion, excluding the bottom two layers, which were fixed to maintain a bulklike structure. This sequential adsorption−relaxation process was continued until a complete monolayer was deposited. TOs for electrodissolution (i.e., the reverse of ED) were calculated starting from a complete adsorbed monolayer and running the deposition procedure in reverse.

Following earlier applications of the TO method,[31,69−87] each deposition or stripping event, inclusively referred to here as a "step," is described by the equilibrium reaction: $(M^{z+} + ze^-) + * \leftrightarrows M^0*$, where M^{z+} represents the metal cation incident upon the metal surface during deposition, the lone

DOI: 10.1021/acsami.8b19787
ACS Appl. Mater. Interfaces 2019, 11, 7954−7964

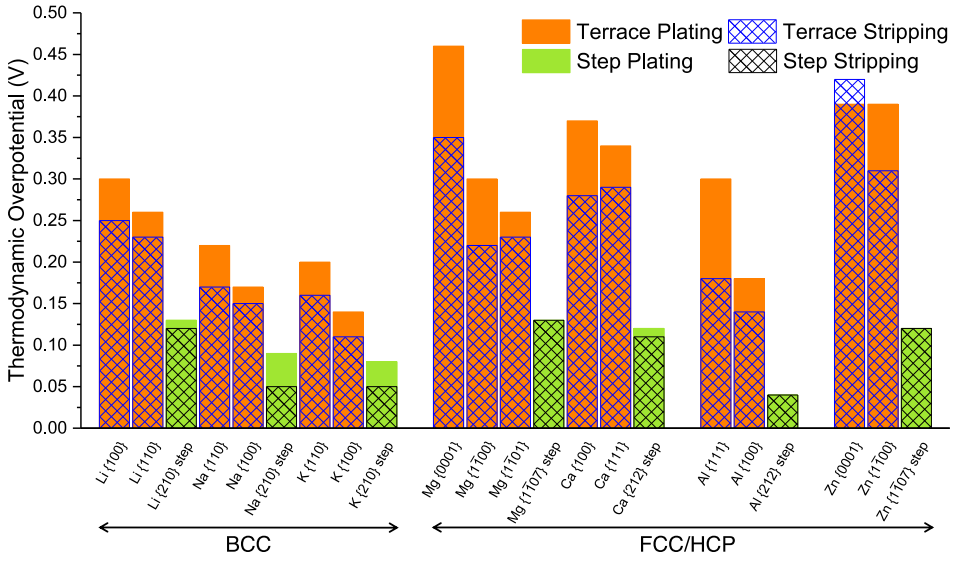

Figure 3. Calculated thermodynamic overpotentials for ED and -dissolution on seven metals as a function of the surface facet and surface morphology (terraces vs steps). Facets of a given metal are arranged according to ascending surface energy, and metals are grouped by columns of the periodic table. Solid orange/green bars represent plating overpotentials on terraces/steps; cross-hatched bars represent stripping overpotentials on terraces and steps. For simplicity, only the absolute value of the overpotential is plotted.

asterisk (*) represents an adsorption site on the surface, z is the oxidation number of the cation, e^- represents an electron, and M^0* is the adsorbed metal adatom after adsorption and reduction.

At equilibrium, the reaction energy associated with each deposition step i in the adsorption sequence is calculated as $\Delta E^{dep}_{rxn,i} = E_i - E_{i-1} - \mu^0$. Here, E_i is the total energy of the surface cell with i metal atoms adsorbed on the surface, E_{i-1} is the energy of the same cell with $i - 1$ adatoms (i.e., from the previous deposition event), and μ^0 is the chemical potential of the bulk metal. Equivalent reaction energies can be defined for the dissolution process, $\Delta E^{diss}_{rxn,i}$. The Nernst equation allows reaction energy to be expressed in terms of potential, U, as

$$U = -\frac{\Delta E_{rxn,i}}{ze} \tag{4}$$

At the equilibrium potential for each metal, the reaction free energy change will in principle vanish, $\Delta E^{dep}_{rxn,i} = \Delta E^{diss}_{rxn,j} = 0$, as there is no net reaction. However, as a result of surface heterogeneity and differences between bonding of adatoms on the surface and within the bulk, $\Delta E^{dep}_{rxn,i}$ and $\Delta E^{diss}_{rxn,i}$ will in general not be equal to zero for each deposition/dissolution event. (Nevertheless, the sum of $\Delta E_{rxn,i}$ and overall deposition/dissolution events that replicate the initial surface structure will be approximately zero. This can be seen by noting that such a sum corresponds to the addition/subtraction of a full monolayer to/from the surface, which is equivalent to increasing/decreasing the thickness of the slab by one bulklike layer.)

Deviations of $\Delta E^{dep}_{rxn,i}$ and $\Delta E^{diss}_{rxn,j}$ from zero are interpreted via eq 4 as thermodynamic contributions to the overpotentials associated with plating or stripping. The most endothermic of these reaction energy changes encountered during the deposition or dissolution process is identified as its respective TO

$$\eta_{dep} = -\left(\frac{\max_i[\Delta E^{dep}_{rxn,i}]}{ze}\right); \quad \eta_{diss} = \left(\frac{\max_i[\Delta E^{diss}_{rxn,i}]}{ze}\right) \tag{5}$$

The sign difference between these two expressions maintains the convention such that plating potentials are negative and stripping potentials are positive.

Deposition/Dissolution on Terraces. Taking the Li{110}, Ca{111}, and Mg{0001} surfaces as examples, Figure 2 plots the partial sums of the reaction energies, $\sum_i \Delta E_{rxn,i}$, for deposition and dissolution as a function of the reaction step. Reading the plots from left to right represents the deposition reaction, whereas reading the plots from right to left represents dissolution. The thick black lines represent the equilibrium condition (i.e., operation at each metal's standard potential). Ideally, and as described above, $\Delta E^{dep}_{rxn,i} = \Delta E^{diss}_{rxn,j} = 0$ for all steps when in equilibrium. This is consistent with a scenario where the local structure of the deposited atom is similar to an atom in the bulk. However, heterogeneity in the surface structure gives rise to nonzero reaction energies. An endothermic reaction step contributes a thermodynamic barrier to the reaction.

Taking deposition on Li{110} as an example, reaction step 1, which represents depositing a single atom onto the pristine surface, has a reaction energy, $\Delta E^{dep}_{rxn,1} = 0.26$ eV. The reaction energy changes for the second, third, and fourth deposition steps are −0.03, 0, and −0.23 eV, respectively. The first deposition step is the most endothermic and represents the limiting step. This step therefore determines the TOs for deposition, $\eta_{dep} = -0.26$ V, eq 5. Application of this potential results in all deposition steps being exothermic, $\Delta E^{dep}_{rxn,i}(V = \eta_{dep}) \leq 0$, dark gray curve; thus, deposition will occur spontaneously under these voltage conditions. Similarly, reading from right to left for dissolution, the first dissolution step $\Delta E^{diss}_{rxn,1} = 0.23$ eV is limiting, thus, $\eta_{diss} = 0.23$ V. Application of a potential equal to 0.23 V results in all dissolution steps being exothermic, $\Delta E^{diss}_{rxn,j}(V = -\eta_{diss}) \leq 0$. This behavior is shown with the light gray curves in Figure 2.

DOI: 10.1021/acsami.8b19787
ACS Appl. Mater. Interfaces 2019, 11, 7954−7964

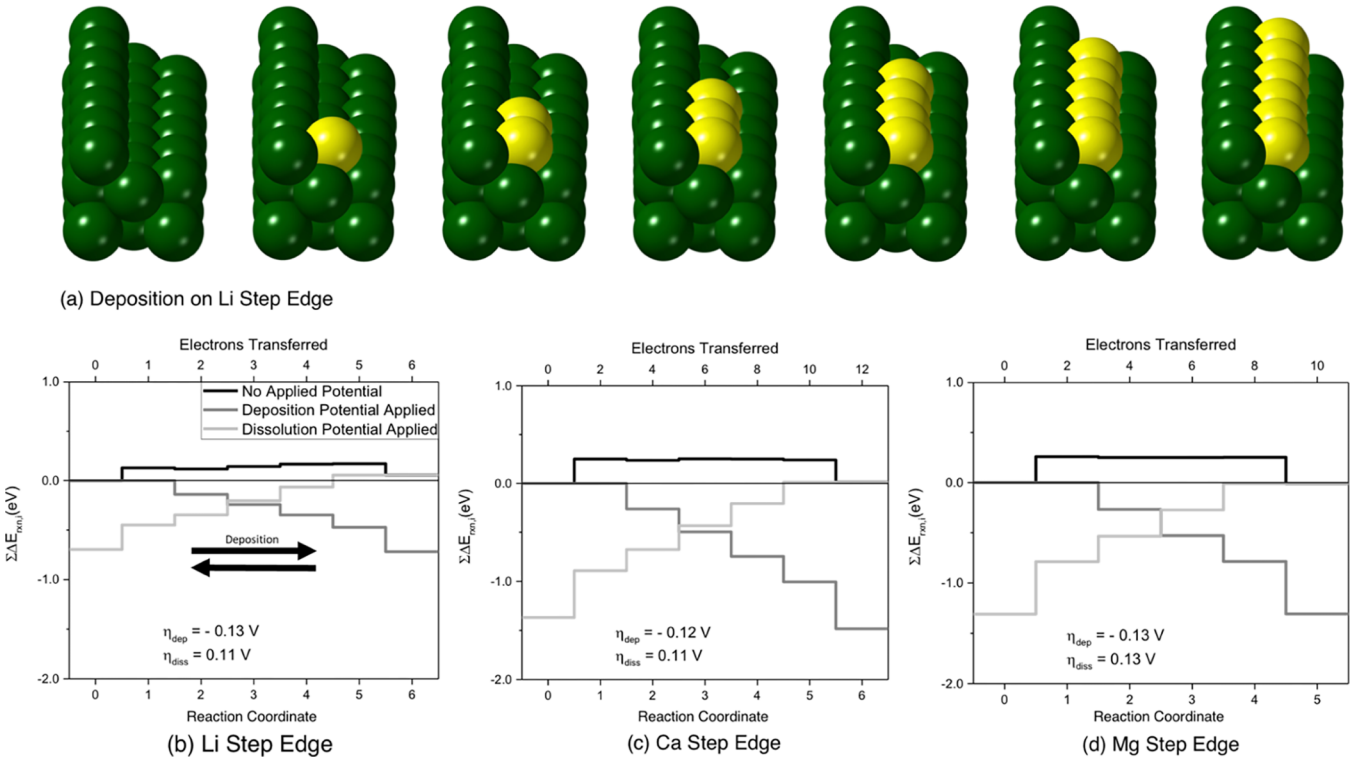

Figure 4. Calculated deposition/dissolution reaction geometries (a) and energies on stepped surfaces of three representative metallic anodes: (b) Li{210}, (c) Ca{212}, and (d) Mg{10$\bar{1}$7}. In panel (a), dark green spheres represent the substrate Li atoms and yellow represents the deposited Li atoms. Atoms are deposited along the step edge until a full row has been completed. (b–d) Reaction energies as a function of the reaction step for three scenarios of applied potential, V:$V = E^0$, represented with the black line, corresponds to the equilibrium potential for a given metal; $V = \eta_{dep}$, dark gray line, corresponds to the potential needed to overcome the thermodynamic overpotential for deposition; and $V = -\eta_{diss}$, light gray line, corresponds to the potential needed to overcome the thermodynamic overpotential for desorption.

Figure 2a–c shows that the initial deposition step onto an empty terrace is consistently the most endergonic step, independent of surface composition. This results from the initial deposition site presenting the least number of nearest neighbors for bonding; this step nucleates a new, single-atom island on top of an existing terrace. Similarly, the final deposition step, 3 → 4, is consistently the most exergonic. This behavior can be explained by the adsorbed species forming a pit in step 3, which subsequently becomes filled upon deposition (step 4). This geometry provides the maximum number of nearest neighbors available to an arriving atom. The reaction energy summed over the entire deposition process is approximately zero, as expected. The reaction energy profile between the initial and final reaction steps exhibits a plateau-like shape with nearly constant reaction energies. These energetic similarities suggest that the plateau reaction steps are structurally similar; indeed, these steps all correspond to deposition/stripping from sites at the edge of the island.

Figure 3 summarizes the TOs across all of the metal surfaces examined. The data are grouped by metal and arranged for a given metal according to increasing surface energy. We first discuss trends in the TO for terrace reactions, represented in Figure 3 by the orange bars (deposition) and overlaid blue cross-hatching (dissolution). Broadly speaking, the calculated TOs on terraces are generally large, ranging from 100 to 500 mV. These values are somewhat larger than those typically observed experimentally at low current densities; see Table S1. As discussed above, this overestimation may be due to the assumption of a terrace-based mechanism, which may not be the preferred experimental adsorption/dissolution site at low rates.

The second trend in the data pertains to the group I metals, Li, Na, and K, which generally exhibit lower TOs compared to the group II metals (Ca and Mg), group III metal (Al), and the transition metal (Zn). This trend is in rough agreement with the experimental overpotentials in Table S1, especially considering that the scan rates for the alkali metals reported there are, on the whole, at least twice those of the group II and group III metals. This trend of less efficient plating in the di- and trivalent metals would be further evident if the reaction energies, $\Delta E_{rxn,i}$, rather than the TOs, were plotted in Figure 3, as this would result in a doubling of the plotted values for the divalent metals and a tripling for trivalent Al.

To explain the lower overpotentials observed for the alkali metals, we recall that they crystallize in the BCC structure, whereas the other metals adopt FCC or HCP lattices. BCC bulk atoms have a coordination number (CN) of 8, whereas for the close-packed FCC and HCP systems, the atoms have CN = 12. Focusing on deposition, we recall that the TO is determined by the initial deposition event. Therefore, the origin of the relatively lower overpotential for the alkali metals should be tied to the bonding environment of these initially deposited adatoms. These adatoms are coordinated by 4 or 5 nearest neighbors on the {110} and {100} surfaces, respectively. In contrast, the CNs for adatoms on the FCC and HCP metals (Mg, Ca, Al, and Zn) are at best similar to the BCC surfaces and are often smaller: CN = 3 on the close-packed {111} and {0001} surfaces; CN = 4 on the FCC {100} surfaces and on Mg {1$\bar{1}$00} and {1$\bar{1}$01}; and CN = 2 on

DOI: 10.1021/acsami.8b19787
ACS Appl. Mater. Interfaces 2019, 11, 7954–7964

Zn{1$\bar{1}$00}. Comparing the bulk CNs to the CNs of the initially deposited adatoms, we note that the BCC alkali metals have the smallest surface-to-bulk CN difference. In other words, the surface bonding environment experienced by the alkali metal adatoms is more similar to their bulklike coordination than in the FCC or HCP systems, as illustrated in Figure S4. We postulate that this similarity results in relatively lower TOs for the alkali metals. A similar argument based on CN has been invoked to explain differences in dendrite formation tendencies during ED of metals.[60]

Additional trends apparent in Figure 3 relate to the surface energy and the asymmetry between deposition and dissolution. Regarding surface energy effects, we note that the TO generally decreases with increasing surface energy. In the case of deposition, this trend can be rationalized by recognizing that the atoms comprising a high-energy facet are more reactive to (i.e., more readily bond with) adatoms. In the case of stripping, and assuming a simple picture of surface energetics that depends only on bond counting, it will be energetically easier to remove an atom (step 4 → 3) from a high surface energy facet because of the fewer bonds that must be broken (relative to a more stable surface). This qualitatively explains the reduction in TOs for stripping on higher surface energy facets.

Deposition/Dissolution on Step Edges. Figure 4 shows the calculated reaction energies for deposition and dissolution on selected stepped surfaces for Li, Ca, and Mg. Data for the other four metals are given in Figures S1−S3. Similar to the energy profile for plating/stripping on terraces, Figure 2, the limiting reaction on stepped surfaces is always the first deposition or stripping event, which corresponds to the nucleation of a kink. An additional similarity with the terraced surfaces is the plateau-like shape of the reaction profile. The reactions comprising the plateau region exhibit similar energies because they all correspond to the same process, that is, propagation of a kink along the step edge.

An important difference between the stepped and terraced surfaces is the magnitude of the TO. For the systems depicted in Figure 4, the TO ranges from −0.13 to 0.13 V. These values are roughly 2−3 times smaller than those for terraces reported in Figure 2. The trend of the stepped surfaces exhibiting significantly smaller TOs is maintained across the other metals, as shown in Figure 3. This trend can be understood using a simple bond-counting argument; adsorption at a step edge or kink presents a larger number of coordinating atoms compared to adsorption on a terrace.

Steady-State Nucleation Rate. In the case of nucleation during the ED process, assuming that the process is controlled by the kinetics of the electrochemical reaction and not by the diffusion of atoms on the surface, the frequency of collision of the atoms with the critical nucleus, ω_c in eq 2, is defined as $S_c i_0/ze$, in which S_c is the surface area of the critical nucleus and i_0 is the exchange current density.[47] Moreover, under an applied potential, U_{app}, the formation energy of the critical nucleus, ΔG_c, can be written as[47]

$$\Delta G_c = -ze(\eta_{dep} - U_{app}) \quad (6)$$

The calculated steady-state nucleation rate and formation energy of the critical nucleus for ED on terrace and step sites at an applied potential of −10 mV are listed in Table S3 of the Supporting Information.

Figure 5 shows the steady-state nucleation rate as a function of applied potential for ED on terrace and step sites obtained

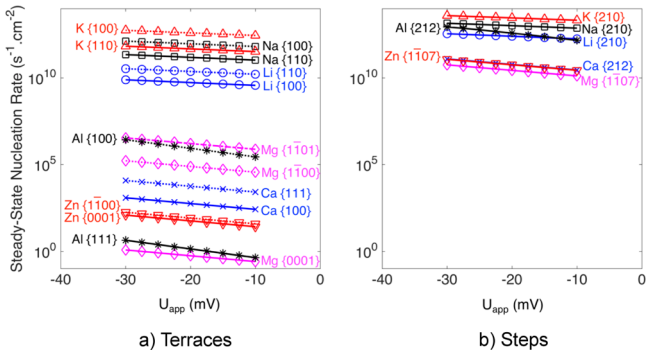

Figure 5. Steady-state nucleation rate as a function of applied potential, U_{app}, for plating on (a) terrace and (b) step sites on seven metal negative electrodes. U_{app} is varied from −30 to −10 mV vs the corresponding equilibrium potential for each metal.

using our calculated TOs as the input to eq 1. The relatively small TOs predicted for the alkali metals (Li, Na, and K) generally result in higher steady-state nucleation rates compared to the other metals, regardless of whether plating occurs on terraces or at steps. However, as discussed earlier and as demonstrated in Figures 2−4, the TO for plating at step sites is smaller than that on terrace sites. This results in a steady-state nucleation rate that is several orders of magnitude higher at steps compared to terrace sites, independent of the choice of metal. This is attributed to the exponential relationship between the reaction energies of initial deposition and the nucleation rate as defined by eq 2. The relative ordering of the surfaces/metals with respect to their nucleation rate is similar for step and terrace deposition sites. Nevertheless, the rates on the step sites are more tightly clustered, suggesting that deposition in these cases is less sensitive to the metal's composition.

Figure 5 also illustrates that the nucleation rate increases with the application of a more negative potential, as expected. The slope of each line is proportional to the number of transferred electrons, z, during the electrochemical reduction of the corresponding metallic ion. By applying a negative potential, U_{app}, the formation energy of the critical nucleus decreases by $|zeU_{app}|$, which exponentially increases the steady-state nucleation rate.

A number of studies argue that the nucleation phenomenon is one of the key parameters that governs how a metal will plate during ED. For example, mesoscale simulations of Li dendrite growth indicate that more uniform deposition (i.e., impingement and subsequent stable growth) can be achieved when nuclei are more densely distributed,[88] as would be afforded by a large population of kink sites on the electrode surface. Experimentally, the role of nucleus density on the plating behavior has been examined by Garcia et al.,[89] who reported the prevention of dendrite formation in Zn metal anodes by introducing a nucleation pulse to increase the initial coverage of Zn nuclei. More recently, Rehnlund et al. showed that dendrite-free Li deposition can be achieved by using a decreased Li salt concentration and a short nucleation pulse, which resulted in an increased nucleus density on the electrode surface.[90]

DOI: 10.1021/acsami.8b19787
ACS Appl. Mater. Interfaces 2019, 11, 7954−7964

CONCLUSIONS

The TOs and associated nucleation rates are calculated for seven metals (Li Na, K, Mg, Ca, Al, and Zn) considered as potential anodes for next-generation rechargeable batteries. The magnitude of the calculated overpotentials is in many cases similar to the measured values and ranges from tens to hundreds of mV. These calculations also provide insight regarding the inefficiencies associated with ED of Ca and Mg; the calculated overpotentials for these metals are amongst the largest overall, consistent with measurements.

We observe that a metal's crystal structure correlates with the efficiency of plating and stripping; body-centered cubic alkali metals are predicted to be among the most efficient systems, whereas the remaining metals, all of which possess close-packed crystal structures, are predicted to have higher TOs. As expected, ED/dissolution is most efficient at kink sites on steps, while undercoordinated terrace sites yield the largest TO. Trends involving surface energies are discussed. Differences between the calculated overpotentials and experimental measurements highlight the importance of kinetic factors (which are not accounted for in the present approach), such as Ohmic resistance in electrolytes, diffusion through solid electrolyte interphases, surface diffusion, electron transfer, etc.

Steady-state nucleation rates were estimated using a classical nucleation model informed by the present DFT calculations. These simulations allow for a comparison of ED nucleation rates on different metallic surfaces and surface features (e.g., terraces vs step edges). The small TOs predicted for plating at step edges result in higher nucleation rates at these features, suggesting that a large population of kink sites will promote efficient cycling. Nucleation rates on terraces differ by several orders of magnitude across the metals, with rates on the body-centered cubic metals predicted to be the fastest. In contrast, nucleation rates at step edges are within a few orders of magnitude of each other, indicating a weak dependence on metal composition. This approach demonstrates a technique for linking atomistic data with a continuum nucleation model, and highlights the sensitivity of the nucleation behavior on the structure and composition of the electrode surface.

ASSOCIATED CONTENT

Supporting Information

The Supporting Information is available free of charge on the ACS Publications website at DOI: 10.1021/acsami.8b19787.

> Experimental overpotentials, bulk properties, plots of calculated deposition/dissolution reaction energies for all surfaces under consideration, plot of reaction energy versus coordination difference, plots of steady-state nucleation rates versus critical formation energy, and plots of steady-state nucleation rates versus surface energy (PDF)

AUTHOR INFORMATION

Corresponding Author

*E-mail: djsiege@umich.edu. Phone: +1 (734) 764-4808.

ORCID

Saeed Kazemiabnavi: 0000-0003-2409-709X

Donald J. Siegel: 0000-0001-7913-2513

Notes

The authors declare no competing financial interest.

ACKNOWLEDGMENTS

This work was supported as part of the Joint Center for Energy Storage Research, an Energy Innovation Hub funded by the U.S. Department of Energy, Office of Science, Basic Energy Sciences. D.J.S. acknowledges support from the U.S. National Science Foundation, grant CBET-1351482.

REFERENCES

(1) Kim, H.; Jeong, G.; Kim, Y.-U.; Kim, J.-H.; Park, C.-M.; Sohn, H.-J. Metallic Anodes for Next Generation Secondary Batteries. *Chem. Soc. Rev.* **2013**, *42*, 9011−9034.

(2) Yoo, H. D.; Shterenberg, I.; Gofer, Y.; Gershinsky, G.; Pour, N.; Aurbach, D. Mg Rechargeable Batteries: An On-Going Challenge. *Energy Environ. Sci.* **2013**, *6*, 2265−2279.

(3) Ellis, B. L.; Nazar, L. F. Sodium and Sodium-Ion Energy Storage Batteries. *Curr. Opin. Solid State Mater. Sci.* **2012**, *16*, 168−177.

(4) Crabtree, G. The Joint Center for Energy Storage Research: A New Paradigm for Battery Research and Development. *AIP Conf. Proc.* **2015**, *1652*, 112−128.

(5) Cox, P. A. *The Elements: Their Origin, Abundance, and Distribution*; Oxford University Press: Oxford, 1989.

(6) Vanysek, P. Electrochemical Series. In *CRC Handbook of Chemistry and Physics*, 96th ed.; Haynes, W. M., Ed.; CRC Press: Boca Raton, FL, 2015.

(7) Huggins, R. A. *Advanced Batteries: Materials Science Aspects*; Springer: New York, 2009.

(8) Brandt, K. Historical Development of Secondary Lithium Batteries. *Solid State Ionics* **1994**, *69*, 173−183.

(9) Tullo, A. H. Batteries That Breathe Air. *C&EN Glob. Enterp.* **2017**, *27*, 21−22.

(10) Aurbach, D.; Lu, Z.; Schechter, A.; Gofer, Y.; Gizbar, H.; Turgeman, R.; Cohen, Y.; Moshkovich, M.; Levi, E. Prototype Systems for Rechargeable Magnesium Batteries. *Nature* **2000**, *407*, 724−727.

(11) Muldoon, J.; Bucur, C. B.; Gregory, T. Quest for Nonaqueous Multivalent Secondary Batteries: Magnesium and Beyond. *Chem. Rev.* **2014**, *114*, 11683−11720.

(12) Zhang, T.; Tao, Z.; Chen, J. Magnesium-air batteries: from principle to application. *Mater. Horiz.* **2014**, *1*, 196−206.

(13) Phinergy Product Page. http://www.phinergy.com/product/. (accessed March 19, 2018).

(14) Matsuda, Y.; ŌOuchi, Y.; Tamura, H. Anodic polarization of aluminium in organic electrolytes. *J. Appl. Electrochem.* **1974**, *4*, 53−56.

(15) Licht, S.; Levitin, G.; Yarnitzky, C.; Tel-Vered, R. The Organic Phase for Aluminum Batteries. *Electrochem. Solid-State Lett.* **1999**, *2*, 262−264.

(16) Nakayama, Y.; Senda, Y.; Kawasaki, H.; Koshitani, N.; Hosoi, S.; Kudo, Y.; Morioka, H.; Nagamine, M. Sulfone-Based Electrolytes for Aluminium Rechargeable Batteries. *Phys. Chem. Chem. Phys.* **2015**, *17*, 5758−5766.

(17) Endres, F. Ionic Liquids: Solvents for the Electrodeposition of Metals and Semiconductors. *ChemPhysChem* **2002**, *3*, 144−154.

(18) Jiang, T.; Brym, M. J. C.; Dubé, G.; Lasia, A.; Brisard, G. M. Electrodeposition of aluminium from ionic liquids: Part I-electrodeposition and surface morphology of aluminium from aluminium chloride (AlCl3)-1-ethyl-3-methylimidazolium chloride ([EMIm]Cl) ionic liquids. *Surf. Coat. Technol.* **2006**, *201*, 1−9.

(19) Jiang, T.; Brym, M. J. C.; Dubé, G.; Lasia, A.; Brisard, G. M. Electrodeposition of aluminium from ionic liquids: Part II—studies on the electrodeposition of aluminum from aluminum chloride (AlCl3)—trimethylphenylammonium chloride (TMPAC) ionic liquids. *Surf. Coat. Technol.* **2006**, *201*, 10−18.

(20) Deng, J.; Luo, W.-B.; Chou, S.-L.; Liu, H.-K.; Dou, S.-X. Sodium-Ion Batteries: From Academic Research to Practical Commercialization. *Adv. Energy Mater.* **2017**, *8*, 1701428.

(21) Hartmann, P.; Bender, C. L.; Vračar, M.; Dürr, A. K.; Garsuch, A.; Janek, J.; Adelhelm, P. A rechargeable room-temperature sodium superoxide (NaO2) battery. *Nat. Mater.* **2012**, *12*, 228−232.
(22) Adelhelm, P.; Hartmann, P.; Bender, C. L.; Busche, M.; Eufinger, C.; Janek, J. From Lithium to Sodium: Cell Chemistry of Room Temperature Sodium-Air and Sodium-Sulfur Batteries. *Beilstein J. Nanotechnol.* **2015**, *6*, 1016−1055.
(23) Ren, X.; Wu, Y. A Low-Overpotential Potassium-Oxygen Battery Based on Potassium Superoxide. *J. Am. Chem. Soc.* **2013**, *135*, 2923−2926.
(24) Zhao, Q.; Hu, Y.; Zhang, K.; Chen, J. Potassium-Sulfur Batteries: A New Member of Room-Temperature Rechargeable Metal-Sulfur Batteries. *Inorg. Chem.* **2014**, *53*, 9000−9005.
(25) Aurbach, D.; Skaletsky, R.; Gofer, Y. The Electrochemical Behavior of Calcium Electrodes in a Few Organic Electrolytes. *J. Electrochem. Soc.* **1991**, *138*, 3536−3545.
(26) Ponrouch, A.; Monti, D.; Boschin, A.; Steen, B.; Johansson, P.; Palacín, M. R. Non-Aqueous Electrolytes for Sodium-Ion Batteries. *J. Mater. Chem. A* **2015**, *3*, 22−42.
(27) Wang, D.; Gao, X.; Chen, Y.; Jin, L.; Kuss, C.; Bruce, P. G. Plating and stripping calcium in an organic electrolyte. *Nat Mater* **2018**, *17*, 16−20.
(28) Liu, Z.; Cui, T.; Pulletikurthi, G.; Lahiri, A.; Carstens, T.; Olschewski, M.; Endres, F. Dendrite-Free Nanocrystalline Zinc Electrodeposition from an Ionic Liquid Containing Nickel Triflate for Rechargeable Zn-Based Batteries. *Angew. Chem., Int. Ed.* **2016**, *55*, 2889−2893.
(29) Chang, H.; Lim, C. Zinc Deposition During Charging Nickel/Zinc Batteries. *J. Power Sources* **1997**, *66*, 115−119.
(30) Paunovic, M.; Schlesinger, M. *Fundamentals of Electrochemical Deposition*; Wiley: Hoboken, N.J., 2006.
(31) Hummelshøj, J. S.; Luntz, A. C.; Norskov, J. K. Theoretical Evidence for Low Kinetic Overpotentials in Li-O_2 Electrochemistry. *J. Chem. Phys.* **2013**, *138*, 034703.
(32) Erdey-Grúz, T.; Volmer, M. Zur Theorie der Wasserstoff Überspannung. *Z. Phys. Chem.* **1930**, *150*, 203−213.
(33) Sahari, A.; Azizi, A.; Schmerber, G.; Dinia, A. Nucleation, Growth, and Morphological Properties of Electrodeposited Nickel Films from Different Baths. *Surf. Rev. Lett.* **2008**, *15*, 717−725.
(34) Willis, M.; Alkire, R. Additive-Assisted Nucleation and Growth by Electrodeposition. *J. Electrochem. Soc.* **2009**, *156*, D377−D384.
(35) Stephens, R. M.; Alkire, R. C. Additive-Assisted Nucleation and Growth by Electrodeposition II. Mathematical Model and Comparison with Experimental Data. *J. Electrochem. Soc.* **2009**, *156*, D385−D394.
(36) Sun, M.; Liao, H.-G.; Niu, K.; Zheng, H. Structural and Morphological Evolution of Lead Dendrites During Electrochemical Migration. *Sci. Rep.* **2013**, *3*, 1−6.
(37) Saidi, W. A. Density Functional Theory Study of Nucleation and Growth of Pt Nanoparticles on MoS_2(001) Surface. *Cryst. Growth Des.* **2015**, *15*, 642−652.
(38) Prestianni, A.; Ferrante, F.; Sulman, E. M.; Duca, D. Density Functional Theory Investigation on the Nucleation and Growth of Small Palladium Clusters on a Hyper-Cross-Linked Polystyrene Matrix. *J. Phys. Chem. C* **2014**, *118*, 21006−21013.
(39) Ferrante, F.; Prestianni, A.; Cortese, R.; Schimmenti, R.; Duca, D. Density Functional Theory Investigation on the Nucleation of Homo- and Heteronuclear Metal Clusters on Defective Graphene. *J. Phys. Chem. C* **2016**, *120*, 12022−12031.
(40) Kohn, W.; Sham, L. J. Self-Consistent Equations Including Exchange and Correlation Effects. *Phys. Rev.* **1965**, *140*, A1133−A1138.
(41) Kresse, G.; Hafner, J. Ab initiomolecular dynamics for liquid metals. *Phys. Rev. B: Condens. Matter Mater. Phys.* **1993**, *47*, 558−561.
(42) Kresse, G.; Furthmüller, J. Efficiency of *ab-initio* Total Energy Calculations for Metals and Semiconductors using a Plane-Wave Basis Set. *Comput. Mater. Sci.* **1996**, *6*, 15−50.
(43) Kresse, G.; Furthmüller, J. Efficient iterative schemes forab initiototal-energy calculations using a plane-wave basis set. *Phys. Rev. B: Condens. Matter Mater. Phys.* **1996**, *54*, 11169−11186.
(44) Kresse, G.; Joubert, D. From Ultrasoft Pseudopotentials to the Projector Augmented-Wave Method. *Phys. Rev. B: Condens. Matter Mater. Phys.* **1999**, *59*, 1758−1775.
(45) Perdew, J. P.; Burke, K.; Ernzerhof, M. Generalized Gradient Approximation Made Simple. *Phys. Rev. Lett.* **1996**, *77*, 3865−3868.
(46) Blöchl, P. E. Projector Augmented-Wave Method. *Phys. Rev. B: Condens. Matter Mater. Phys.* **1994**, *50*, 17953−17979.
(47) Gamburg, Y. D.; Zangari, G. *Theory and Practice of Metal Electrodeposition*; Springer: New York, 2011.
(48) Toschev, S.; Markov, I. Transient Nucleation in Electrodeposition of Mercury. *J. Cryst. Growth* **1968**, *3-4*, 436−440.
(49) Balluffi, R. W.; Allen, S. M.; Carter, W. C.; Kemper, R. A. *Kinetics of Materials*; Wiley-Interscience: Hoboken, N.J., 2005.
(50) Murnaghan, F. D. The Compressibility of Media Under Extreme Pressures. *Proc. Natl. Acad. Sci. U.S.A.* **1944**, *30*, 244−247.
(51) Ledbetter, H. M. Elastic Properties of Zinc: A Compilation and a Review. *J. Phys. Chem. Ref. Data* **1977**, *6*, 1181−1203.
(52) Fiorentini, V.; Methfessel, M. Extracting Convergent Surface Energies from Slab Calculations. *J. Phys.: Condens. Matter* **1996**, *8*, 6525−6529.
(53) Feldbauer, G.; Wolloch, M.; Bedolla, P. O.; Mohn, P.; Redinger, J.; Vernes, A. Adhesion and Material Transfer Between Contacting Al and TiN Surfaces from First Principles. *Phys. Rev. B: Condens. Matter Mater. Phys.* **2015**, *91*, 165413.
(54) Tran, R.; Xu, Z.; Radhakrishnan, B.; Winston, D.; Sun, W. H.; Persson, K. A.; Ong, S. P. Surface Energies of Elemental Crystals. *Sci. Data* **2016**, *3*, 160080.
(55) Tyson, W. R.; Miller, W. A. Surface Free Energies of Solid Metals: Estimation from Liquid Surface Tension Measurements. *Surf. Sci.* **1977**, *62*, 267−276.
(56) de Boer, F. R.; Boom, R.; Mattens, W. C. M.; Miedema, A. R.; Niessen, A. K. *Cohesion in Metals: Transition Metal Alloys*; North-Holland: Amsterdam, 1988.
(57) Tyson, W. R. Surface Energies of Solid Metals. *Can. Metall. Q.* **1975**, *14*, 307−314.
(58) Wang, J.; Wang, S.-Q. Surface Energy and Work Function of FCC and BCC Crystals: Density Functional Study. *Surf. Sci.* **2014**, *630*, 216−224.
(59) Fu, J.; Zhang, C.; Zhao, J. Gupta Potential for Alkaline Earth Metals: Calcium and Strontium. *Comput. Mater. Sci.* **2014**, *85*, 142−146.
(60) Jäckle, M.; Groß, A. Microscopic Properties of Lithium, Sodium, and Magnesium Battery Anode Materials Related to Possible Dendrite Growth. *J. Chem. Phys.* **2014**, *141*, 174710.
(61) Kohn, W.; Mattsson, A. E. Edge Electron Gas. *Phys. Rev. Lett.* **1998**, *81*, 3487−3490.
(62) Mattsson, A. E.; Kohn, W. An Energy Functional for Surfaces. *J. Chem. Phys.* **2001**, *115*, 3441−3443.
(63) Mattsson, T. R.; Mattsson, A. E. Calculating the Vacancy Formation Energy in Metals: Pt, Pd, and Mo. *Phys. Rev. B: Condens. Matter Mater. Phys.* **2002**, *66*, 214110.
(64) Mattsson, A. E.; Armiento, R.; Schultz, P. A.; Mattsson, T. R. Nonequivalence of the Generalized Gradient Approximations PBE and PW91. *Phys. Rev. B: Condens. Matter Mater. Phys.* **2006**, *73*, 195123.
(65) Zucker, R. V.; Chatain, D.; Dahmen, U.; Hagège, S.; Carter, W. C. New Software Tools for the Calculation and Display of Isolated and Attached Interfacial-Energy Minimizing Particle Shapes. *J. Mater. Sci.* **2012**, *47*, 8290−8302.
(66) Miedema, A. R. Surface Energies of Solid Metals. *Z. Metallkde.* **1978**, *69*, 287−292.
(67) Miedema, A. R.; Boom, R. Surface-Tension and Electron-Density of Pure Liquid-Metals. *Z. Metallkde.* **1978**, *69*, 183−190.
(68) Hayun, S.; Tran, T.; Ushakov, S. V.; Thron, A. M.; van Benthem, K.; Navrotsky, A.; Castro, R. H. R. Experimental Methodologies for Assessing the Surface Energy of Highly

DOI: 10.1021/acsami.8b19787
ACS Appl. Mater. Interfaces 2019, 11, 7954−7964

Hygroscopic Materials: The Case of Nanocrystalline Magnesia. *J. Phys. Chem. C* **2011**, *115*, 23929−23935.
(69) Smith, J. G.; Naruse, J.; Hiramatsu, H.; Siegel, D. J. Theoretical Limiting Potentials in Mg/O2 Batteries. *Chem. Mater.* **2016**, *28*, 1390−1401.
(70) Nørskov, J. K.; Rossmeisl, J.; Logadottir, A.; Lindqvist, L.; Kitchin, J. R.; Bligaard, T.; Jónsson, H. Origin of the Overpotential for Oxygen Reduction at a Fuel-Cell Cathode. *J. Phys. Chem. B* **2004**, *108*, 17886−17892.
(71) Rossmeisl, J.; Qu, Z.-W.; Zhu, H.; Kroes, G.-J.; Nørskov, J. K. Electrolysis of Water on Oxide Surfaces. *J. Electroanal. Chem.* **2007**, *607*, 83−89.
(72) Man, I. C.; Su, H.-Y.; Calle-Vallejo, F.; Hansen, H. A.; Martínez, J. I.; Inoglu, N. G.; Kitchin, J.; Jaramillo, T. F.; Nørskov, J. K.; Rossmeisl, J. Universality in Oxygen Evolution Electrocatalysis on Oxide Surfaces. *ChemCatChem* **2011**, *3*, 1159−1165.
(73) Viswanathan, V.; Hansen, H. A.; Rossmeisl, J.; Nørskov, J. K. Universality in Oxygen Reduction Electrocatalysis on Metal Surfaces. *ACS Catal.* **2012**, *2*, 1654−1660.
(74) Mukherjee, J.; Linic, S. First-Principles Investigations of Electrochemical Oxidation of Hydrogen at Solid Oxide Fuel Cell Operating Conditions. *J. Electrochem. Soc.* **2007**, *154*, B919−B924.
(75) Ingram, D. B.; Linic, S. First-Principles Analysis of the Activity of Transition and Noble Metals in the Direct Utilization of Hydrocarbon Fuels at Solid Oxide Fuel Cell Operating Conditions. *J. Electrochem. Soc.* **2009**, *156*, B1457−B1465.
(76) Peterson, A. A.; Abild-Pedersen, F.; Studt, F.; Rossmeisl, J.; Nørskov, J. K. How Copper Catalyzes the Electroreduction of Carbon Dioxide into Hydrocarbon Fuels. *Energy Environ. Sci.* **2010**, *3*, 1311−1315.
(77) Durand, W. J.; Peterson, A. A.; Studt, F.; Abild-Pedersen, F.; Nørskov, J. K. Structure Effects on the Energetics of the Electrochemical Reduction of CO_2 by Copper Surfaces. *Surf. Sci.* **2011**, *605*, 1354−1359.
(78) Tang, W.; Peterson, A. A.; Varela, A. S.; Jovanov, Z. P.; Bech, L.; Durand, W. J.; Dahl, S.; Nørskov, J. K.; Chorkendorff, I. The Importance of Surface Morphology in Controlling the Selectivity of Polycrystalline Copper for CO_2 Electroreduction. *Phys. Chem. Chem. Phys.* **2012**, *14*, 76−81.
(79) Girishkumar, G.; McCloskey, B.; Luntz, A. C.; Swanson, S.; Wilcke, W. Lithium−Air Battery: Promise and Challenges. *J. Phys. Chem. Lett.* **2010**, *1*, 2193−2203.
(80) Hummelshøj, J. S.; Blomqvist, J.; Datta, S.; Vegge, T.; Rossmeisl, J.; Thygesen, K. S.; Luntz, A. C.; Jacobsen, K. W.; Nørskov, J. K. Communications: Elementary Oxygen Electrode Reactions in the Aprotic Li-Air Battery. *J. Chem. Phys.* **2010**, *132*, 071101.
(81) Mo, Y.; Ong, S. P.; Ceder, G. First-Principles Study of the Oxygen Evolution Reaction of Lithium Peroxide in the Lithium-Air Battery. *Phys. Rev. B: Condens. Matter Mater. Phys.* **2011**, *84*, 205446.
(82) Viswanathan, V.; Thygesen, K. S.; Hummelshøj, J. S.; Nørskov, J. K.; Girishkumar, G.; McCloskey, B. D.; Luntz, A. C. Electrical Conductivity in Li_2O_2 and Its Role in Determining Capacity Limitations in Non-Aqueous Li-O_2 Batteries. *J. Chem. Phys.* **2011**, *135*, 214704.
(83) Siahrostami, S.; Tripković, V.; Lundgaard, K. T.; Jensen, K. E.; Hansen, H. A.; Hummelshøj, J. S.; Mýrdal, J. S. G.; Vegge, T.; Nørskov, J. K.; Rossmeisl, J. First Principles Investigation of Zinc-Anode Dissolution in Zinc-Air Batteries. *Phys. Chem. Chem. Phys.* **2013**, *15*, 6416−6421.
(84) Viswanathan, V.; Nørskov, J. K.; Speidel, A.; Scheffler, R.; Gowda, S.; Luntz, A. C. Li-O_2 Kinetic Overpotentials: Tafel Plots from Experiment and First-Principles Theory. *J. Phys. Chem. Lett.* **2013**, *4*, 556−560.
(85) Lee, B.; Seo, D.-H.; Lim, H.-D.; Park, I.; Park, K.-Y.; Kim, J.; Kang, K. First-Principles Study of the Reaction Mechanism in Sodium-Oxygen Batteries. *Chem. Mater.* **2014**, *26*, 1048−1055.
(86) Chen, L. D.; Nørskov, J. K.; Luntz, A. C. Al-Air Batteries: Fundamental Thermodynamic Limitations from First-Principles Theory. *J. Phys. Chem. Lett.* **2014**, *6*, 175−179.
(87) Chen, L. D.; Nørskov, J. K.; Luntz, A. C. Theoretical Limits to the Anode Potential in Aqueous Mg-Air Batteries. *J. Phys. Chem. C* **2015**, *119*, 19660−19667.
(88) Enrique, R. A.; DeWitt, S.; Thornton, K. Morphological Stability During Electrodeposition. *MRS Commun.* **2017**, *7*, 658−663.
(89) Garcia, G.; Ventosa, E.; Schuhmann, W. Complete Prevention of Dendrite Formation in Zn Metal Anodes by Means of Pulsed Charging Protocols. *ACS Appl. Mater. Interfaces* **2017**, *9*, 18691−18698.
(90) Rehnlund, D.; Ihrfors, C.; Maibach, J.; Nyholm, L. Dendrite-Free Lithium Electrode Cycling via Controlled Nucleation in Low $LiPF_6$ Concentration Electrolytes. *Mater. Today* **2018**, *21*, 1010−1018.

DOI: 10.1021/acsami.8b19787
ACS Appl. Mater. Interfaces 2019, 11, 7954−7964